Contents lists available at ScienceDirect

Optics and Lasers in Engineering

journal homepage: www.elsevier.com/locate/optlaseng

Jacobi–Fourier phase mask for wavefront coding

E. González-Amador [a,*], A. Padilla-Vivanco [b], C. Toxqui-Quitl [b], J. Arines [c], E. Acosta [a]

[a] *Departamento de Física aplicada, Facultad de Física, Campus Vida, Universidad de Santiago de Compostela, 15782 España*
[b] *Universidad Politécnica de Tulancingo, Ingenierías No. 100, 43629, Tulancingo, Hidalgo, México*
[c] *Departamento de Física aplicada, Facultad de Óptica y Optometría, Campus Vida, Universidad de Santiago de Compostela, 15782 España*

ARTICLE INFO

ABSTRACT

In this work we propose Jacobi–Fourier phase masks for wavefront coding-based imaging systems. The optical properties of the phase mask is study in detail and numerical simulation are shown. Pixel size and noise are taken into account for the deconvolution of images. Numerical simulations indicate that overall performance is better than of the well-known and commonly used trefoil phase.

1. Introduction

Wavefront coding (WFC) is a hybrid optical-computational technique that makes use of a phase modulating element in conjunction with a deconvolution algorithm to extend the depth of field or depth of focus of a digital imaging system [1–3].

The most obvious way to extend the depth of focus is to decrease the aperture; However, this reduces the resolution of the system due to diffraction and energy reduction at the sensor [4,5]. The other approach is to deconvolve the defocused images in order to deblur the out of focus regions. This approach has two main problems:

a) the response to the system (PSF) is not invariant under focus shifts and is therefore not known in most of the cases and,
b) deconvolution is an ill posed problem due to the loss of information for those special frequencies where the MTF is close or equal to zero [6–9].

Many solutions have been proposed to achieve this goal, in recent decades within the field called engineering in the pupil. One of them, the technique known as WFC developed by Dowski and Cathey [1] proposes the simple placement of a phase mask (PM) at the exit pupil of the optical system that generates a controlled amount of third order aberrations. The PM must be able to generate a PSF that is invariant within a desired range of defocus and its corresponding MTF must also be free of zeroes within the interval of spatial frequencies that the optical system was designed to detect [6]. Many other shapes deriving from the original cubic phase mask solution [1], have been proposed for some specific imaging systems. The most representative of these are: root square [7], trefoil [10], sinusoidal [11] free-form [12], exponential [13], tangential [14], logarithmic [15,16], rational [17] and many others phase

modulation shapes. PM in the shape of linear combinations of Zernike polynomials have been also studied [8,18,19].

WFC has been successfully applied in different fields as infrared imaging [9], optical design to reduce complexity of optical systems [18,20], microscopy [21], retinal imaging [22,23] among others.

As we pointed out above, one of the requirements for the deconvolution process to be effective is that the MTF has not zeros. In general, most of the MTFs used for WFC based optical systems obey this condition, but they show a sudden decay from the origin, what implies a loss of contrast in comparison with diffraction-limited optical systems. However, the deconvolution process compensates this problem and the processed images show, in general, an acceptable contrast for the required depth of field and resolution [5–8]. Even so, not all phases perform with the same quality in the final results.

Recently, Nhu et al. [7] showed that the good performance of a root square shaped PM is due to the smooth shape of the phase generated in the central part of the pupil and to a rapid variation at the periphery that leads to non-zero and stable MTFs when defocusing. Based on this premise, in this study we look at the performance of PM in the shape of Jacobi–Fourier (JF) and will find which one of them fits with this behavior and can be used for WFC.

This work is organized as follows: In Section 2 we briefly introduce the mathematical description and properties of the JFP, and in the Section 3 we search for polynomials that are smooth in the center and steep in the periphery and propose some that meet the criteria for its validation in the following sections.

In Section 4 we analyze the optical properties of JF phase mask (JFPM) and explain the decoding algorithms used to get the simulated images. Section 5 is devoted to show, analyze and discuss the results. Lastly, in Section 6 we present the conclusions.

---

* Corresponding author.
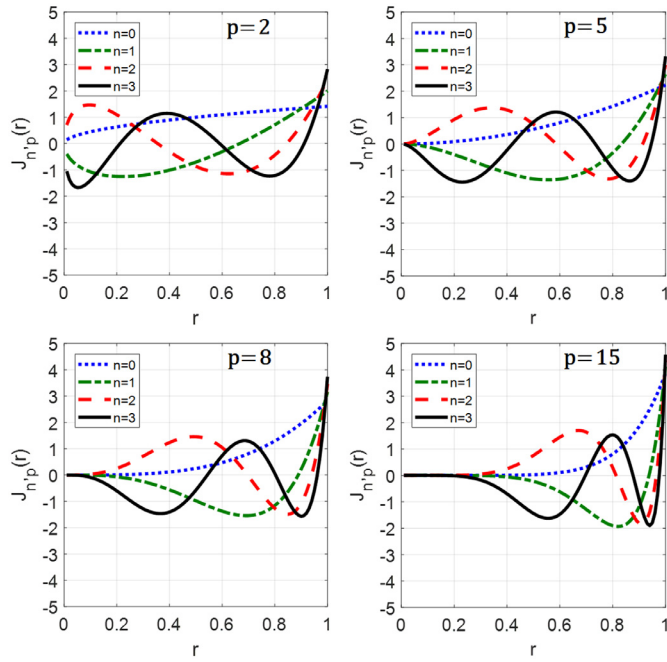*E-mail address:* enrique.gonzalez.amador@rai.usc.es (E. González-Amador).

E. González-Amador, A. Padilla-Vivanco and C. Toxqui-Quitl et al.

Optics and Lasers in Engineering 126 (2020) 105880

Fig. 1. Behavior of the radial Jacobi polynomials with n and p.

Table 1
Radial dependence of JFPM.

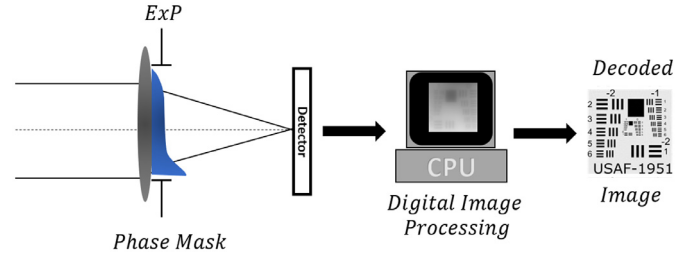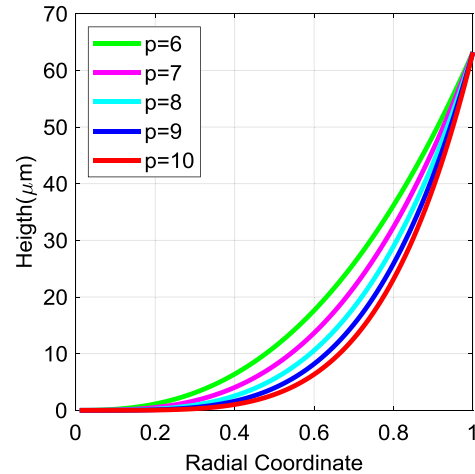| p	Radial dependence
6	$\sqrt{6}r^{5/2}$
7	$\sqrt{7}r^3$
8	$\sqrt{8}r^{7/2}$
9	$\sqrt{9}r^4$
10	$\sqrt{10}r^{9/2}$

Fig. 2. Diagram of wavefront coding imaging system used.

Fig. 3. Radial phase profiles of the phase mask.

2. Jacobi–Fourier polynomials

Jacobi polynomials, $G_n(p, q, r)$, are a class of classic orthogonal polynomials in the interval [0,1], where $n \geq 0$ indexes the set of orthogonal polynomials for given p and q values, and the independent variable r will represent in this work the radial coordinate normalized to the pupil radius [24].

The orthonormal Jacobi radial polynomials used in this work are defined by [25]

$$J_n(p, q, r) = \sqrt{\frac{w(p,q,r)}{b_n(p,q)}} G_n(p, q, r), \quad (1)$$

where $w(p, q, r)$ is the weighting function, and $b_n(p, q)$ the normalization factor. The parameters p and q must obey $(p - q) > -1$ and $q > 0$; these expressions are calculated as follows [24,26],

$$G_n(p, q, r) = \frac{n!(q-1)!}{(p+n-1)!} \sum_{s=0}^{n} (-1)^s \frac{(p+n+s-1)!}{(n-s)!s!(q+s-1)!} r^s \quad (2)$$

$$b_n(p, q) = \frac{n![(q-1)!]^2(p-q+n)!}{(q-1+n)!(p-1+n)!(p+2n)}, \quad (3)$$

$$w(p, q, r) = (1-r)^{p-q} r^{q-1}. \quad (4)$$

The shifted Legendre, Mellin, and shifted Chebyshev polynomials are special cases of $G_n(p, q, r)$ [27].

The Jacobi polynomials are chosen as the radial function, hence Jacobi–Fourier polynomials (JFP) $P_{nm}(p, q, r, \theta)$, are defined as [25],

$$P_{nm}(p, q, r, \theta) = J_n(p, q, r) \exp im\theta. \quad (5)$$

For our purposes, in this work we will consider real polynomials and we will use the following expression for the phase masks:

$$P_{nm}(p, q, r, \theta) = J_n(p, q, r) \cos(m\theta + \theta_0), \quad (6)$$

where θ is the azimuthal angle, θ_0 denotes the angle of rotated JPF and $m \geq 0$ the azimuthal frequency. We must stress the fact that not all combinations of m, p and q provide 2D polynomials separable in the x and y coordinates.

3. Choice of Jacobi–Fourier polynomials

First, we restricted all infinite possible sets of JFP to those with integer values of p and q and $p = q$. Other choices for these two parameters could also be considered and we do not claim that ours necessarily perform better than others. The primary aim of this work is to show that JFP shaped phase masks can be used in WFC optical systems. Other families of JFP will be the subject of future works. Considering that $p = q$ we decided to denote the radial Jacobi polynomials as $J_{n,p}(r)$.

In Fig. 1 we present the profiles of different JFP obtained with the combinations $p = [2, 5, 8, 15]$ and $n = [0, 1, 2, 3]$. We observe that as n increases the number of ripples increases and hence the smooth region needed in the central part of the pupil cannot be achieved. Moreover, for values of p equal to or less than 5, the smooth flat central region is very small or none existent and therefore we restrict our study to p values equal to or greater than 6.

As we explained in the introduction, we adhere to the assumption that a phase with smooth slopes in the center of the pupil and steep slopes at the periphery gives rise to defocus invariant MTFs leading to good resolution images [7]. We therefore initially selected $n = 0$ and $p \geq 6$. Also, we disregarded values of $p > 10$ because, as we will show, they decrease the depth of focus. Thus, our study for the radial part of
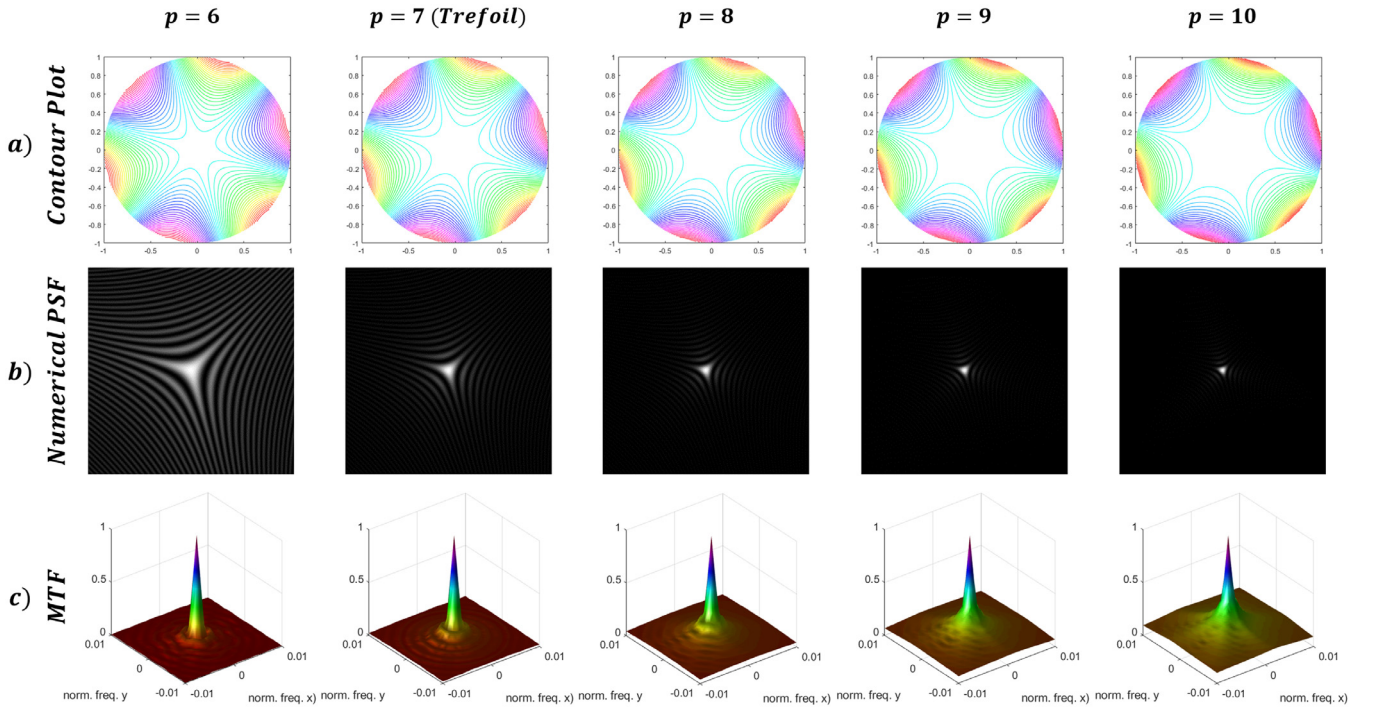
Fig. 4. (a) 2D Phase maps, (b) simulated PSF for the proposed JFPM and trefoil PM, (c) 3D MTF for JFPM and Trefoil PM.

the JFP is restricted to $n = 0$ and $6 \leq p \leq 10$. Table 1 shows the radial dependence of the chosen JFPM, $J_{n,p}(r)$.

As for the choice of azimuthal frequency, for even values of m, JFPM behave as astigmatism aberration and the spatial resolution of the decoded images is poor. Odd values of m perform better. For $m = 1$ they extent the depth of focus in the same way as coma [28] but this is not as effective as trefoil, $m = 3$ [10,20]. Moreover, when $p = 7$ and $m = 3$ JFP becomes trefoil aberration (Zernike polynomial Z_3^3) which has been shown to perform better than the pure cubic mask originally proposed by Dowski [19], and hence the results for the JFPM proposed here will be compared with those for trefoil one.

4. Optical properties of JFPM and decoding algorithms

For the numerical analysis we considered an optical system consisting of a lens with a focal length of 25 mm and pupil diameter of 10 mm. The object is set at infinity with a wavelength of 632 nm. Also, we assume that the JFPM is placed at the lens plane. The general scheme is shown in the Fig. 2. We illustrate the results with the object at infinity for simplicity, but the numerical analysis is also valid for any set of conjugated planes.

The generalized pupil function $\Pi_{n,p}(r, \theta)$ [29] for the optical system can be expressed as:

$$\Pi_{n,p}(r, \theta) = \begin{cases} \exp[ik\, \phi_{n,p}(r,\theta)] & if \; r \leq 1 \\ 0 & \text{otherwise} \end{cases}, \tag{7}$$

where

$$\phi_{n,p}(r, \theta) = \alpha r^{\frac{p-1}{2}} \cos\left(3\theta - \pi/4\right) + W_{20} r^2, \tag{8}$$

and α denotes the strength of the phase, $k = 2\pi/\lambda$ is the wave number, λ the wavelength and r the radius of the lens which has been normalized to unity. Since we are not interested in the orthogonality properties of Jacobi Polynomials, we have normalized them to unity, in this way all they provide the same peak to valley (PV) values for the same strength α. W_{20} represents the amount of defocus due to either a mispositioning of the image plane or the object plane. $-\pi/4$ is added to the angular

coordinate to rotate the point spread function (PSF) in the image plane in order to reduce artifacts in the restored image.

The system's PSF was computed by evaluating the square modulus of the discrete Fourier Transform of the optical pupil function. The optical transfer function (OTF) was computed as the inverse discrete Fourier Transform of the PSF [30]. FFT evaluations were performed by routines provided by Matlab and sampling of the pupil plane on a grid of 4096×4096 pixels in order to avoid undesirable numerical artifacts. We determined a pixel size at the image plane of $0.79\,\mu m$ in order to work in the limit of the Nyquist theorem [30].

In Fig. 3 we show the profiles of the different radial Jacobi polynomials obtained with $p = [6, 7, 8, 9, 10]$ and $\alpha = 100\lambda$. We can see how by changing the p value we are able to increase or decrease the extension of the central plateau of the phase masks.

Fig. 4a shows the corresponding 2D contour maps of the different phase masks, while Fig. 4b shows the corresponding in-focus PSFs. We can also observe on the contour maps that the extension of the plateau increases as p increase and hence smaller PSFs. Fig. 4c shows the in-focus corresponding 3D modulation transfer functions (MTF). It can be observed that for small values of p the MTFs show ripples at low frequencies. As p increases the MTFs become smoother.

4.1. Analysis of optical properties of PM

In this section, with the primary aim of comparing the performance of the JFPM, we will analyze both MTFs and phase transfer functions (PTF) in X direction within a defocus interval of 5λ, $W_{20} \in [0, 5\lambda]$, and two values of the strength, $\alpha = 50\lambda$ and $\alpha = 100\lambda$. Owing to the symmetry of the problem, results are also valid for the interval $[-5\lambda, 5\lambda]$. In Fig. 5 we plot the optical MTFs, denoted as $MTF(\alpha, W_{20})$, as well as the system MTFs, $MTF_{System}(\alpha, W_{20})$, defined as:

$$MTF_{System}(\alpha, W_{20}) = \frac{MTF(\alpha, W_{20})}{MTF(\alpha, 0)}, \tag{9}$$

We can observe that in all cases $MTF(\alpha, W_{20})$ have not zeroes, and therefore deconvolution is not going to be an ill posed problem. For a
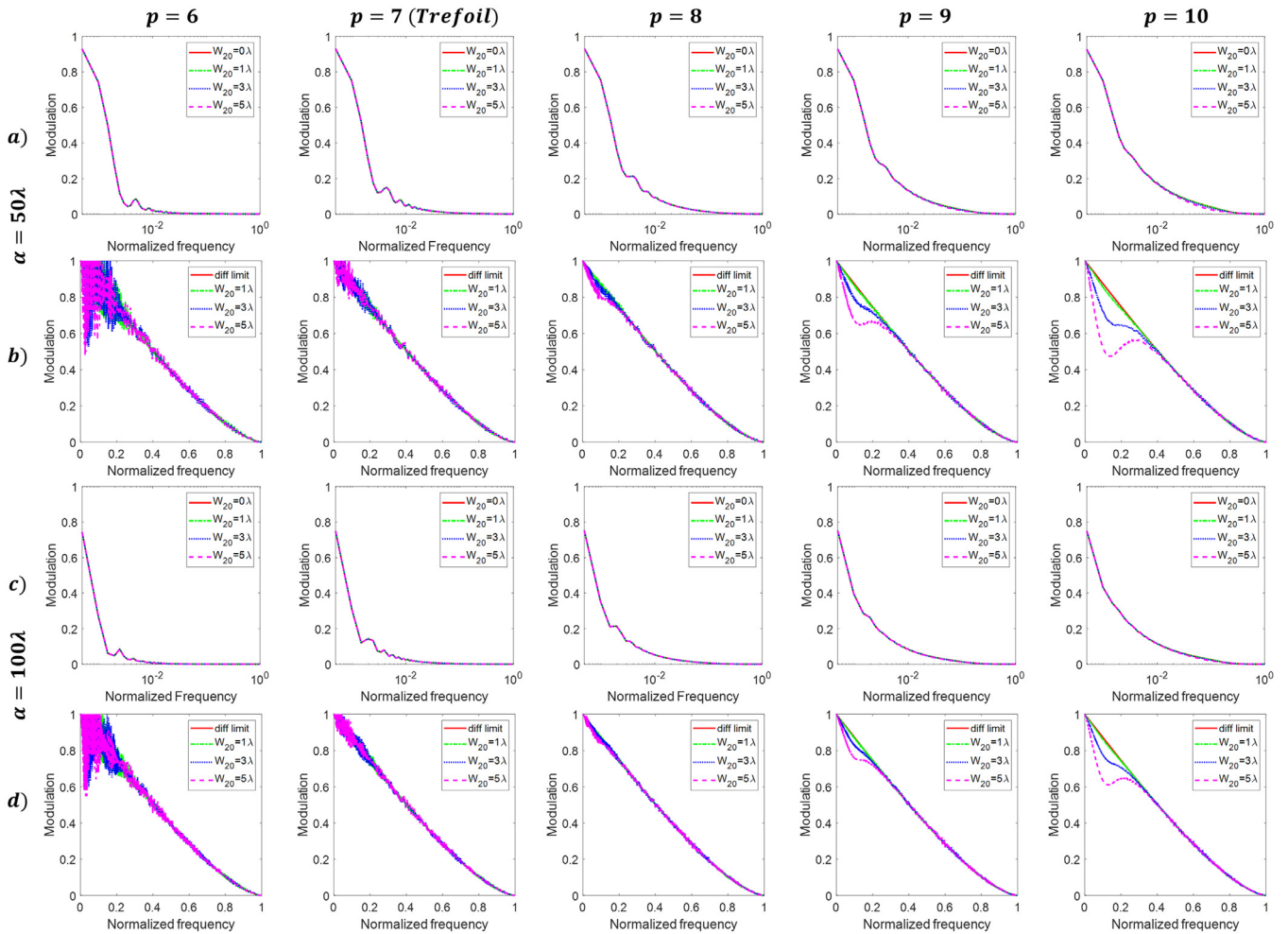
Fig. 5. (a) $MTF(\alpha, W_{20})$ corresponding to the different PM and defocus magnitudes for $\alpha = 50\lambda$. (b) $MTF_{\text{System}}(\alpha, W_{20})$ corresponding to the different JFPM and defocus magnitudes for $\alpha = 50\lambda$. (c) $MTF(\alpha, W_{20})$ corresponding to the different PM and defocus magnitudes for $\alpha = 100\lambda$. (d) $MTF_{\text{System}}(\alpha, W_{20})$ corresponding to the different JFPM and defocus magnitudes for $\alpha = 100\lambda$.

given α, as p increases the amplitude of the $MTF(\alpha, W_{20})$ increases, this will have an impact on the signal to noise ratio of the coded images, and therefore, on the quality of the decoded images. On the other hand, as p increases there is a loss of invariance in the defocus range, i.e., the defocus interval is smaller. All $MTF(\alpha, W_{20})$ show ripples or oscillations. The number and height of oscillations decreases as p increases. This behavior is more evident in the plots of the $MTF_{\text{System}}(\alpha, W_{20})$.

The amplitudes of MTFs decrease and MTF curves become closer with the increase of α.

In recent works it has been shown that artifacts are due to PTF behaviors [31,32]. Therefore, we do also include in this section an analysis of the PTFs. In Fig. 6 we show the PTFs of the system, $PTF_{\text{System}}(\alpha, W_{20})$, defined as:

$$PTF_{\text{System}}(\alpha, W_{20}) = PTF(\alpha, W_{20}) - PTF(\alpha, 0), \qquad (10)$$

We can observe that for a given p and a defocus value, as α increases the PTFs becomes smaller. For a given α, PTFs approach to zero as defocus decreases, as expected. The behavior is clearly dependent on p. $p = 6$ and $p = 7$ show an almost linear dependence between PTFs and frequencies. This relationship changes from $p = 8$, where PTFs are steeper at small frequencies and change this behavior to become smooth functions that approach asymptotically to a value. This value is closer to zero as p and α increases. All plots show ripples. Nevertheless, for small p values, ripples are distributed along all frequencies, being higher at

small frequencies, whereas for bigger p values oscillations are smaller and displace towards high frequencies.

4.2. Image simulation. Decoding algorithms

In previous sections we describe the optical properties of the different JFPM. In this section we will present simulated decoded images for the axial interval $[0, 5\lambda]$. As explained in the preceding section, we sampled the image plane at the limit of the Nyquist Theorem with a pixel size of $0.79\,\mu$m. In the next section, numerical simulations of decoded images of a 1951 USAF target were performed considering a more realistic pixel size. Simulations were performed as per ref [33]:

1) Image codification at high sampling rate;
2) Image downsampling by factor 4, resizing the 4096 × 4096 pixels image to a 1024 × 0124 pixels, i.e., a pixel size of 3.16 μm;
3) Noise adding. In order to analyze the performance of the mask in presence of noise we added to the intermediate coded images random Gaussian noise, with zero mean and three different values of standard deviation: 0.06%, 0.2% and 1%, of the maximum value of the gray level of the optically coded image.
4) Fourier transform of the image;
5) Zero padding of the Image Spectrum by adding a frame of zeros in order to build a matrix of 4096 × 4096 pixels;
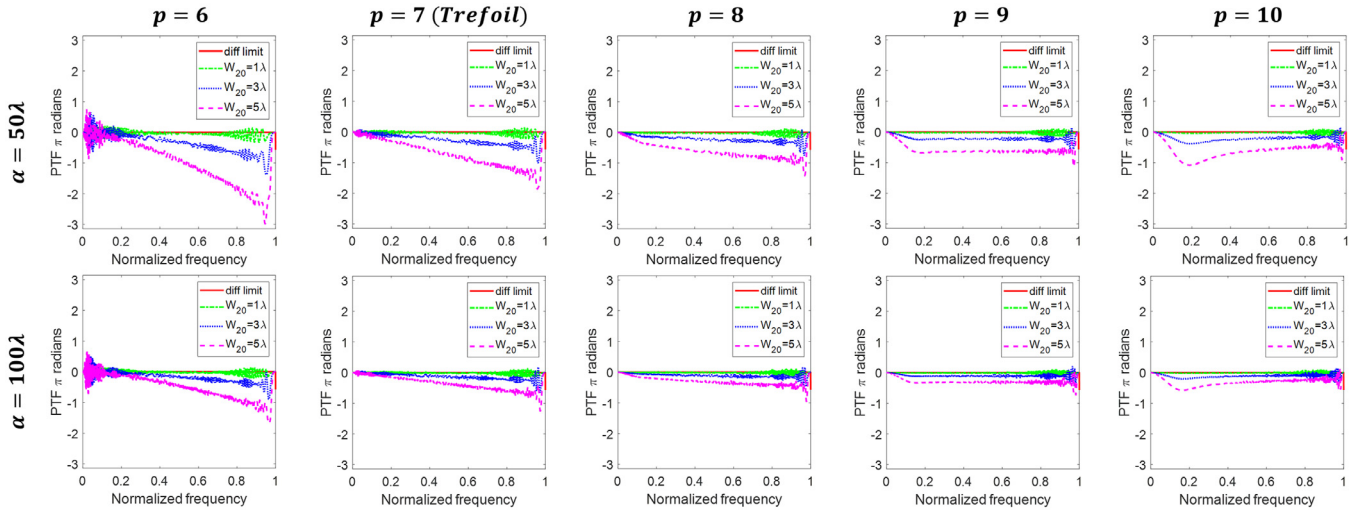6) Application of the Wiener Filter;

E. González-Amador, A. Padilla-Vivanco and C. Toxqui-Quitl et al.

Optics and Lasers in Engineering 126 (2020) 105880

Fig. 6. (a) PTFs of system for $\alpha = 50\lambda$ and $\alpha = 100\lambda$.
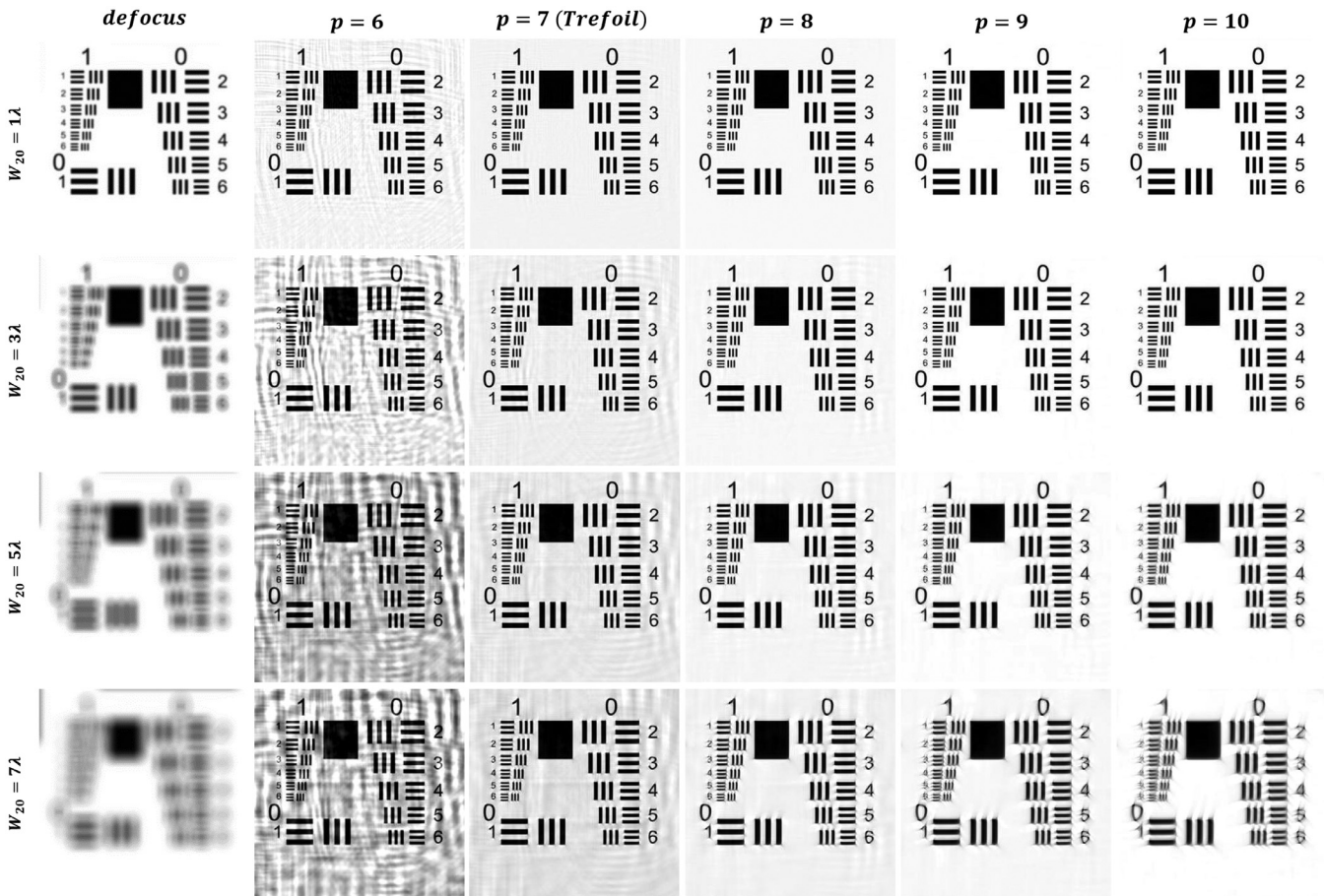

Fig. 7. Decoded images in the absence of noise obtained with the different phase masks and different amounts of defocus in the range $(1\lambda, 7\lambda)$ for $\alpha = 50\lambda$.

7) Inverse Fourier Transform of the Decoded Image Spectrum;
8) Final Decoded Image is downsampled by 2×2 pixel binning.

As stated above, the image restoration was by means of the Wiener Filter [34]. We used values for the regularization parameter, γ within the interval $[10^{-10}, 10^{-3}]$ in order to avoid the deconvolution filter falls below the noise floor or noise will be amplified in the final image. Thus, the spectrum of the decoded image ($\hat{I}_{\text{dec}}$) was derived from the follow-

ing equation:

$$\hat{I}_{\text{dec}} = \frac{\hat{I}_{\text{cod}}(\alpha, W_{20}) \cdot OTF^*(\alpha, 0)}{|OTF(\alpha, 0)|^2 + \gamma} \tag{11}$$

where $\hat{I}_{\text{cod}}(\alpha, W_{20})$ is the spectrum of the defocused coded images and $OTF(\alpha, 0)$ is the in-focus Optical Transfer Function.

It is important to note that only contrast and brightness were adjusted in the decoded images without the use of any other filter.
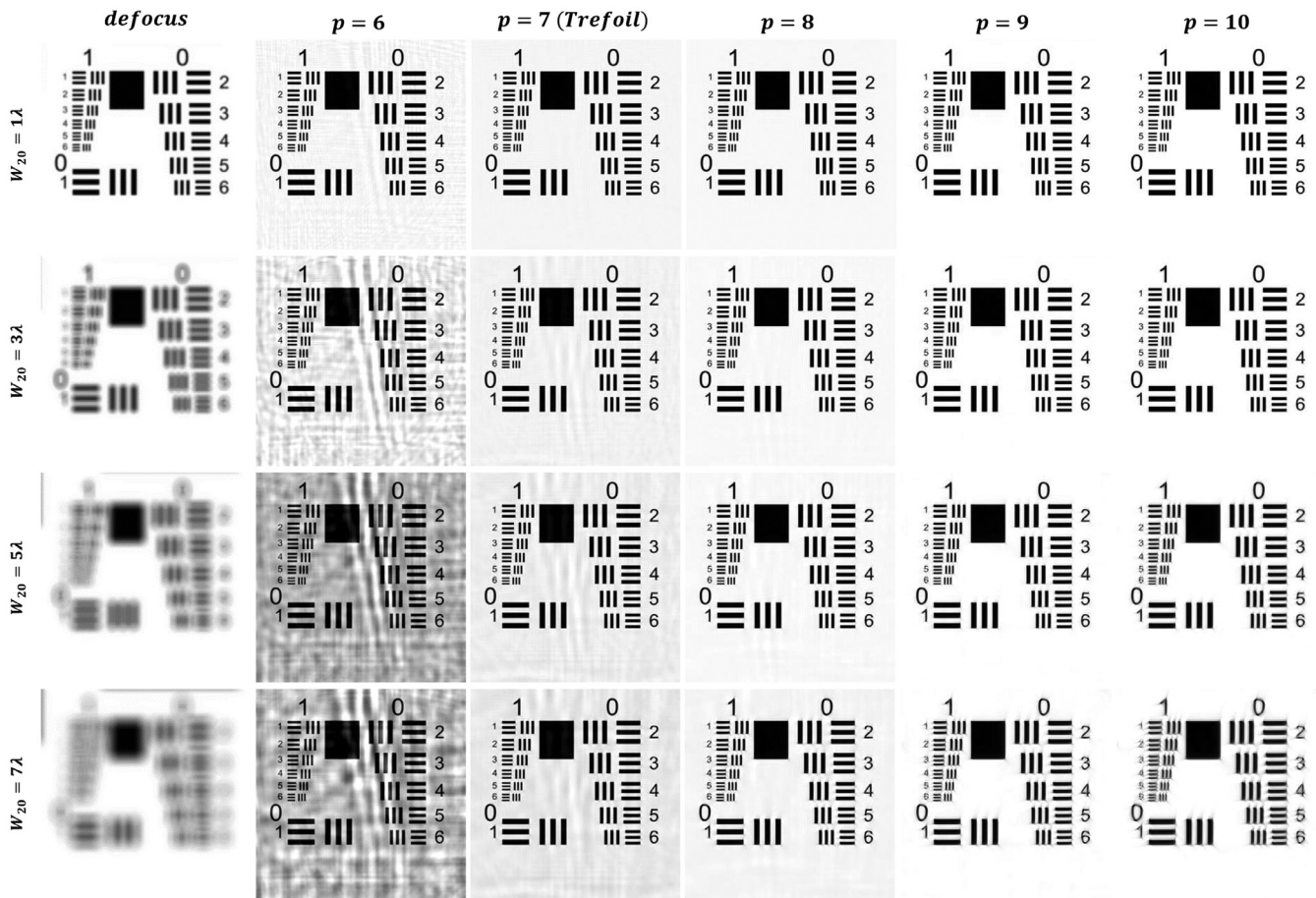
E. González-Amador, A. Padilla-Vivanco and C. Toxqui-Quitl et al.

Optics and Lasers in Engineering 126 (2020) 105880

Fig. 8. Decoded images in absence of noise obtained with the different phase masks and different amounts of defocus in the range $(1\lambda, 7\lambda)$ for $\alpha = 100\lambda$.

5. Results

5.1. Image simulation

Figs. 7 and 8 show simulated images of the 1951 USAF target for the noise-free case when $\alpha = 50\lambda$ and $\alpha = 100\lambda$ respectively. Simulations are made beyond the chosen defocus interval, up to 7λ.

For comparison purposes, we also show the corresponding defocused images when there is no mask in the optical system.

Figs. 9 and 10 shows the results for different levels of noise for defocus 1λ and 5λ when $\alpha = 50\lambda$ and $\alpha = 100\lambda$ respectively.

In all figures the size of the group of bars are G1 + E6 (Group 1, Element 6) = 9.48 μm and G0 + E1 (Group 0, Element 1) = 28.44 μm.

5.2. Discussion

In the noiseless simulations we can observe from Figs. 7 and 8, that images for $p = 6$ show quite prominent artifacts ruining the image quality. For $p = 7$ and in less degree for $p = 8$ some artifacts remain for large defocus, what reduce the image quality; nevertheless, the depth of focus for $p = 7$ goes beyond the considered interval, achieving also sharp results up to 7λ of defocus. Simulations for $p = 9$ and $p = 10$ show neglectable amounts or no artifacts, being contrast and resolution still acceptable, but depth of focus can't be extended beyond the interval $[-5\lambda, 5\lambda]$, and this is due to the lack of invariance of the MTF's as explained in previous section. Moreover, for $p = 9$ and $p = 10$ some defects can be observed at the corners of the bars. And the edges of the bars are no longer too sharp. The higher value of α is the less artifacts present in the images.

From Fig. 6 and in agreement with Demenikov et al. [32] and Mo et al. [31], we can assume that oscillations in the PTF's are the responsible of artifacts in the images. Artifacts due to oscillations in the high frequencies not noticeable because the MTFs are close to zero. For $p = 6$ and $p = 7$ show high oscillations in the PTF's for low frequencies whereas for higher values of p oscillations for low frequencies become very smooth or none and therefore artifacts are not noticeable. Invariance in the PTF's or linearity seems not to be important in what artifacts refer. Distance between PTFs for different amounts of defocus translate into a shift and number of replicas of the artifacts, what depends on the value of α.

Presence and amount of artifacts is also reflected in the system MTFs (Fig. 5b and d) which show strong ripples for the low frequencies for $p = 6$ and 7 and they are smooth for $p = 8$, 9 and 10. The lack of invariance at low frequencies translate in loss of resolution .

When noise is taken into account it can be observed that grainy images are obtained. The amount of grain for a given level of noise decreases with p. More grain implies less details in images. Therefore, the range of defocus for small p values shrinks. The greater the value of α the grainier the images. All these results agree with the fact that the area under the $MTF(\alpha, W_{20})$ increases as p increases and/or α decreases. Noise softens artifacts but they are still visible for $p = 6$ and 7 for small defocus.

Therefore, from our point of view and for the optical system we have considered, the JFPM with $p = 8$ is the one that provides the best images in the noiseless and small level of noise cases; $p = 9$ for medium levels of noise and $p = 10$ for the highest level of noise here simulated.

Finally, point out that by increasing the $F/\#$ in an optical system the DOF could be also increased at expenses of reducing the light gathering capacity of the lens. In the noiseless case a $F/\# = 12.50$ is needed for a
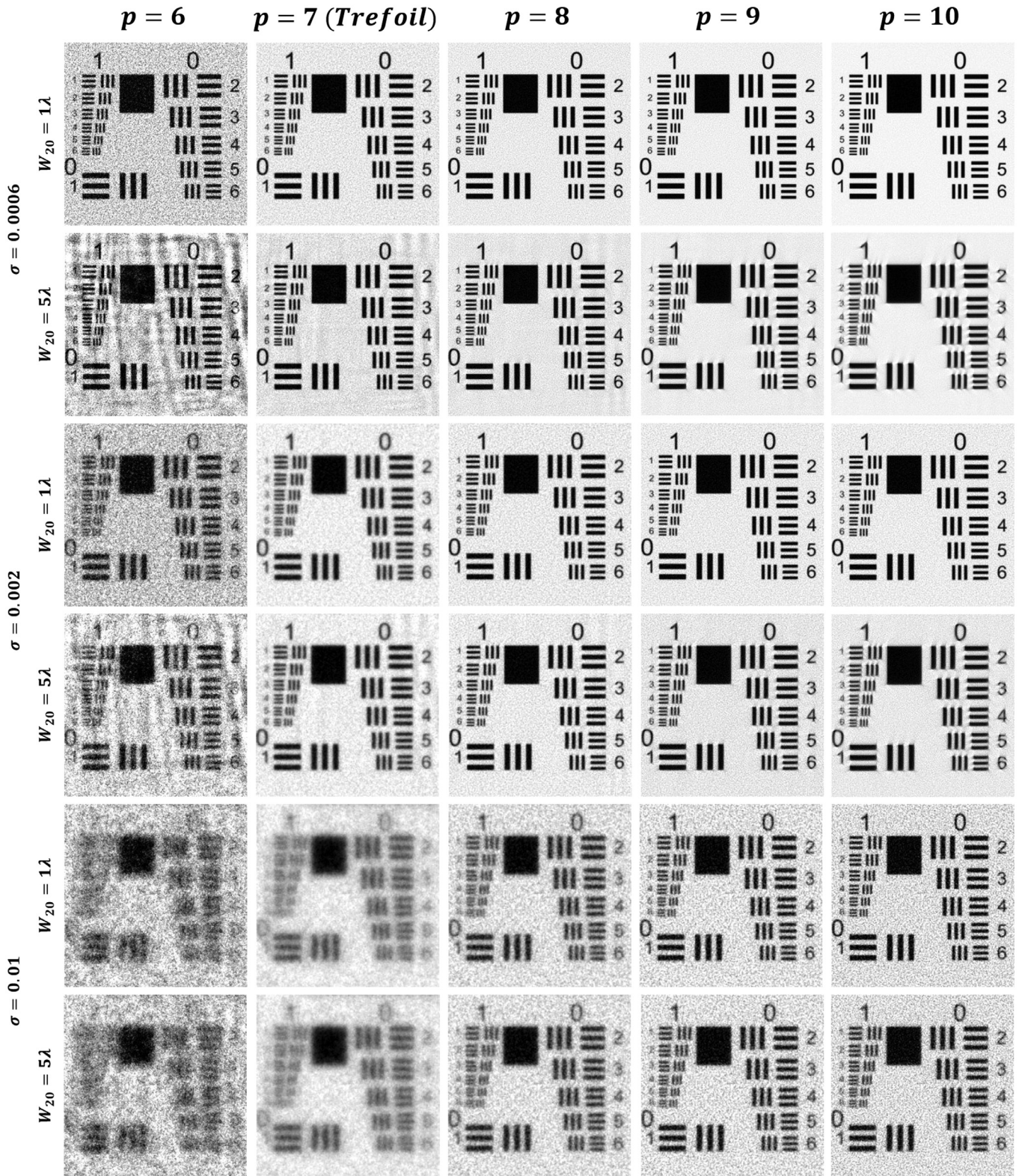
E. González-Amador, A. Padilla-Vivanco and C. Toxqui-Quitl et al.

Optics and Lasers in Engineering 126 (2020) 105880

Fig. 9. Decoded images in presence of different amounts of noise and different amounts of defocus in the range $(1\lambda, 5\lambda)$ for $\alpha = 50\lambda$.

same image quality with a defocus of 5λ. Image degradation, when stopping down the aperture, depends mainly on the recording device. If a CCD is used, then photon noise, dark noise, and read noise must be considered in the SNR calculation. Moreover, different CCDs show different SNR even for same pixel size. Here, in order to simulate the effects of

what reduction of gathering light implies, we will assume the following relationship between SNR for different $F/\#s$ [35], what assumes SNR is inversely proportional to the square of the $F/\#$, thus

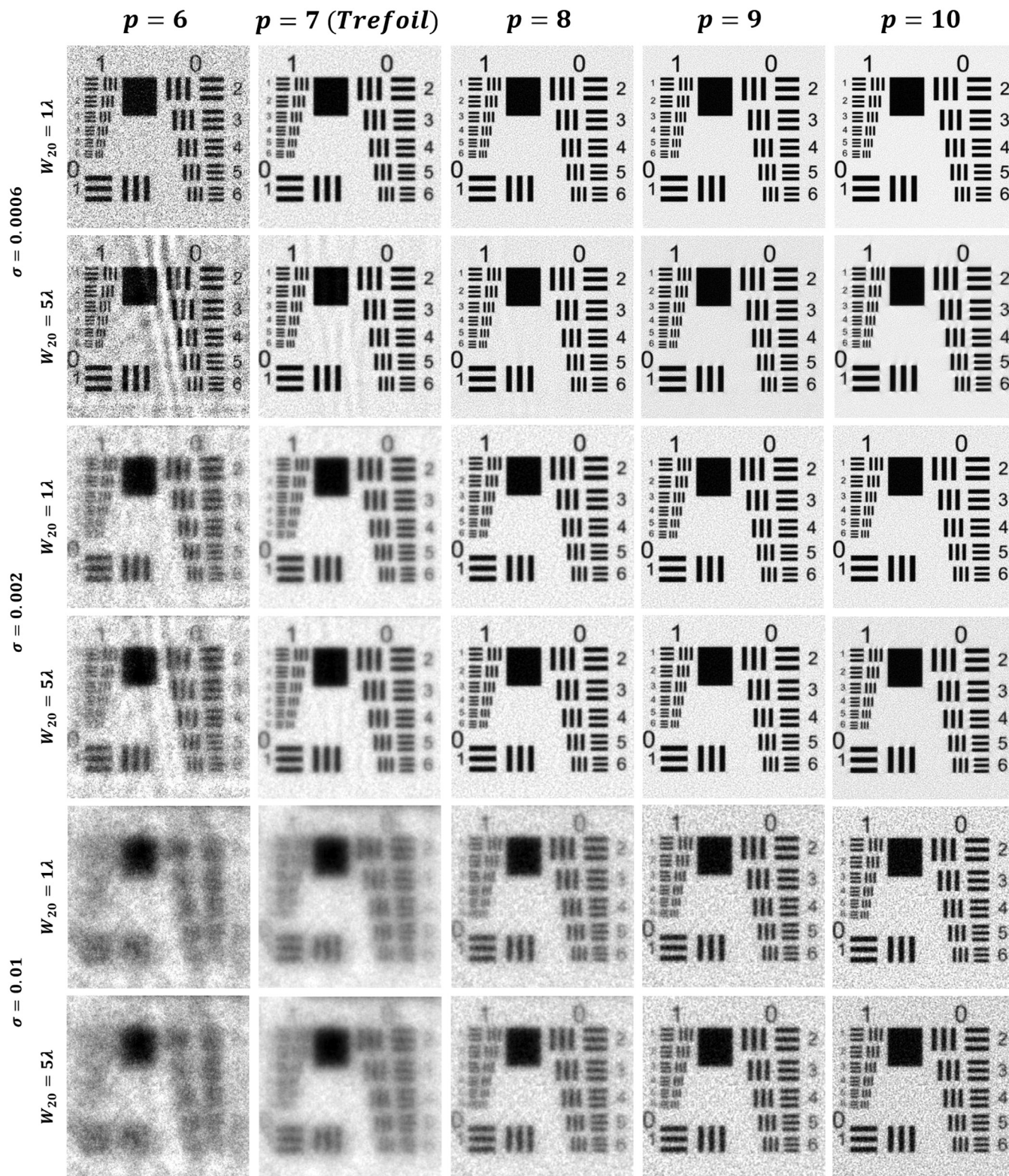$$SNR_{12.5} = SNR_{2.5}\left(\frac{2.5}{12.5}\right)^2, \tag{12}$$

Fig. 10. Decoded images in presence of different amounts of noise and different amounts of defocus in the range $(1\lambda, 5\lambda)$ for $\alpha = 100\lambda$.

In Fig. 11, simulations of images with 5λ defocus for an optical system with $F/\# = 2.50$ and JFPM with $p = 10$ and a defocused optical system with $F/\# = 12.50$ are shown (assuming same exposure time in both cases). First row shows the degradation of the coded images for SNR=37.5, 75 (same as used for simulation in Fig. 10 with $\sigma = 0.01$) and 300. The second row shows the corresponding results for $F/\# = 12.50$. Clearly, wavefront coded images show better resolution and they are less grainy for lower SNR values. For higher values, WFC images are less sharp but show less grain. Of course, noise is amplified by the deconvolution algorithm and there will be a lower limit for the SNR value from which wavefront coding technique is not efficient. [36].
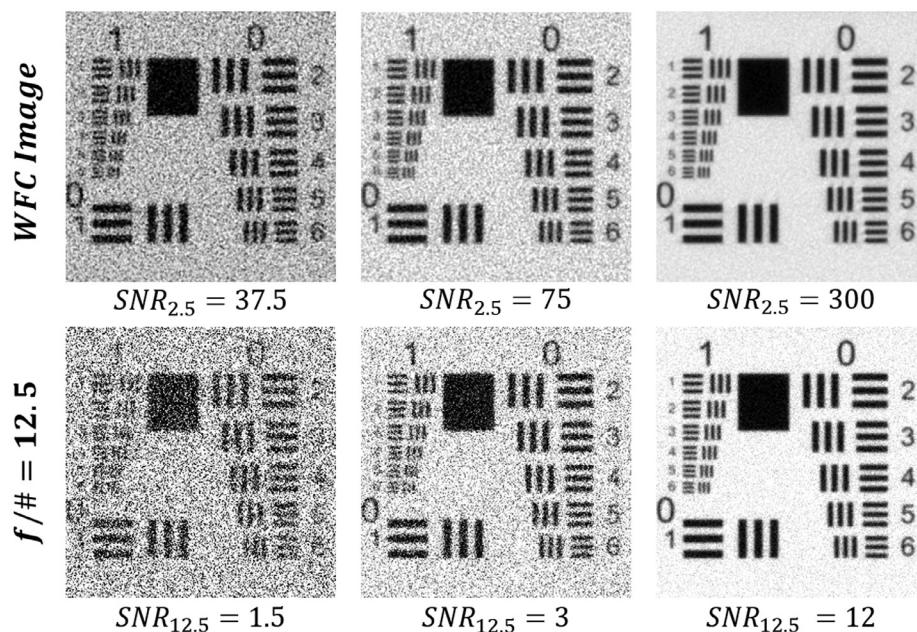
E. González-Amador, A. Padilla-Vivanco and C. Toxqui-Quitl et al.

Optics and Lasers in Engineering 126 (2020) 105880

Fig. 11. Simulated images with a defocus of 5λ and different SNR values for the respective relative apertures. Upper row for WFC with $p = 10$. Lower row with $F/\# = 12.5$. Each column represents the same experimental noise conditions.

6. Conclusions

In this work we explore the use of the Jacobi–Fourier phase masks to extend the depth of focus in an optical imaging system. For the radial part we used Jacobi polynomials, $J_{n,\,p}(r)$ with integer indexes. For the azimuthal dependence, we used $\cos(3\theta)$ in order to be able to draw comparisons with the well-known trefoil phase mask used for wavefront coding. In order to get a smooth central region in the masks, we used only $n = 0$ Jacobi polynomials. For $p = 7$ JFPM become trefoil PM.

The optical system we use to simulate the performance of these masks is a lens of 10 mm diameter and 25 mm focal length ($F/\# = 2.50$). Results are shown for two different mask strengths that provide focus invariance within the interval $[-5\lambda, 5\lambda]$.

We found that values of p smaller than or equal to 7 yield decoded images with artifacts, the smaller the p value the higher the amount of artifacts. $p = 8$ performs the best for the noiseless case or for very low levels of noise and but does not enable the extension of depth of focus beyond the defocus interval. For higher level of noise, p values over 8 perform better, i.e. the higher the noise the higher the p value performs better. These results agree with the analysis of the MTF curves. For small values of p, the curves have ripples which result in the presence of artifacts in the decoded images. Larger p value give rise to softer curves and hence fewer artifacts or none at all. The higher the p value the higher the MTF values and hence the best behavior in the presence of noise. However, invariance is gradually lost as p increases, which implies that as the value of p increases, depth of focus decreases. In other words, the proper choice of the p value is a trade-off among signal to noise ratio, desired depth of focus and presence of artifacts for a given $F/\#$ of the optical system.

In any case, we can conclude that JFPM are good candidates to obtain high resolution images in wavefront coding optical systems.

Acknowledgments

References

[1] Dowski ER, Cathey WT. Extended depth of field through wave-front coding. Appl Opt 1995;34(11):1859–66.

[2] Dowski ER, Johnson GE. Wavefront coding: a modern method of achieving high-performance and/or low-cost imaging systems. In: Current developments in optical design and optical engineering VIII. Proc SPIE, 3779; 1999. p. 137–46.

[3] Cathey WT, Dowski ER. New paradigm for imaging systems. Appl Opt 2002;41(29):6080–92.

[4] Bagheri S, Silveira PE, de Farias DP. Analytical optimal solution of the extension of the depth of field using cubic-phase wavefront coding. Part I. Reduced-complexity approximate representation of the modulation transfer function. JOSA A 2008;25(5):1051–63.

[5] Ferran C, Bosch S, Carnicer A. Design of optical systems with extended depth of field: an educational approach to wavefront coding techniques. IEEE Trans Educ 2012;55(2):271–8.

[6] Carles G. Analysis of the cubic-phase wavefront-coding function: physical insight and selection of optimal coding strength. Opt Laser Eng 2012;50(10):1377–82.

[7] Nhu V, Fan Z, Minh NP, Chen S. Optimized square-root phase mask to generate defocus-invariant modulation transfer function in hybrid imaging systems. Opt Eng 2015;54(3):035103.

[8] Palillero-Sandoval O, Aguilar JF, Berriel-Valdos LR. Phase mask coded with the superposition of four Zernike polynomials for extending the depth of field in an imaging system. Appl Opt 2014;53(18):4033–8.

[9] Muyo G, Singh A, Andersson M, Huckridge D, Wood A, Harvey AR. Infrared imaging with a wavefront-coded singlet lens. Opt Express 2009;17(23):21118–23.

[10] Prasad S, Torgersen TC, Pauca VP, Plemmons RJ, van der Gracht J. Engineering the pupil phase to improve image quality. In: Visual information processing XII. Proc SPIE, 5108; 2003. p. 1–13.

[11] Zhao H, Li Y. Analytical and experimental demonstration of depth of field extension for incoherent imaging system with a standard sinusoidal phase mask. Chinese Opt Lett 2012;10(3):031101.

[12] Takahashi Y, Komatsu S. Optimized free-form phase mask for extension of depth of field in wavefront-coded imaging. Opt Lett 2008;33(13):1515–17.

[13] Yang Q, Liu L, Sun J. Optimized phase pupil masks for extended depth of field. Opt Comm 2007;272(1):56–66.

[14] Chen S, Fan Z. Optimized asymmetrical tangent phase mask to obtain defocus invariant modulation transfer function in incoherent imaging systems. Opt Lett 2014;39(7):2171–4.

[15] Zhao H, Li Y. Performance of an improved logarithmic phase mask with optimized parameters in a wavefront-coding system. Appl Opt 2010;49(2):229–38.

[16] Zhao H, Li Y. Optimized logarithmic phase masks used to generate defocus invariant modulation transfer function for wavefront coding system. Opt Lett 2010;35(15):2630–2.

[17] Zhou F, Li G, Zhang H, Wang D. Rational phase mask to extend the depth of field in optical-digital hybrid imaging systems. Opt Lett 2009;34(3):380–2.

[18] Acosta E. Adaptive phase plates for optical encoding systems invariant to second-order aberrations. Opt Comm 2011;284(16-17):3862–6.

[19] Prasad S, Torgersen T, Pauca VP, Plemmons R. Integrated optics systems for image quality control. In: Proc. AMOS technical conf; 2002.

[20] Kubala K, Dowski E, Cathey WT. Reducing complexity in computational imaging systems. Opt Express 2003;11(18):2102–8.

[21] Arnison MR, Cogswell CJ, Sheppard CJ, Török P. Wavefront coding fluorescence microscopy using high aperture lenses. Opt Imag Micr 2003;87:143–65.

[22] Acosta E, Arines J. Optical-digital system invariant to eye aberrations for retinal imaging. Inv Ophthalmol Visual Sci 2012;53(14) 3098–3098.

[23] Arines J, Hernandez RO, Sinzinger S, Grewe A, Acosta E. Wavefront-coding technique for inexpensive and robust retinal imaging. Opt Lett 2014;39(13): 3986–3988.

[24] Bhatia AB, Wolf E. On the circle polynomials of Zernike and related orthogonal sets. Math Proc Cambridge Philos Soc 1954;50(1):40–8.

[25] Camacho-Bello C, Toxqui-Quitl C, Padilla-Vivanco A, Báez-Rojas JJ. High-precision and fast computation of Jacobi–Fourier moments for image description. JOSA A 2014;31(1):124–34.

[26] Born M, Wolf E. Principles of optics: electromagnetic theory of propagation, interference and diffraction of light. Oxford: Pergamon Press; 1970.

[27] Abramowitz M, Stegun IA. Handbook of mathematical functions: with formulas, graphs, and mathematical tables.. Dover, New York: Ninth Dover Printing, Tenth GPO Printing Edition; 1954.

[28] Dorronsoro C, Guerrero-Colon JA, Marta C, Infante JM, Portilla J. Low-cost wavefront coding using coma and a denoising-based deconvolution. In: Current develop-ments electro-optical and infrared system technology and applications IV. Proc SPIE, 6737; 2007. p. 67370E.

[29] Goodman JW. Introduction to Fourier optics. McGraw-Hill; 1968.

[30] Voelz DG. Computational Fourier optics: a Matlab tutorial. Bellingham, WA: SPIE Press; 2011.

[31] Mo X., Wang J. Phase transfer function based method to alleviate image artifacts in wavefront coding imaging system. In International symposium on photoelectronic detection and imaging 2013: infrared imaging and applications. Proc SPIE 8907 89074H.

[32] Demenikov M, Harvey AR. Image artifacts in hybrid imaging systems with a cubic phase mask. Opt Express 2010;18(8):8207–12.

[33] Scrymgeour DA, Adelsberger K, Boye R. Advanced imaging optics utilizing wavefront coding. Sandia National Lab.; 2015. (SNL-NM).

[34] Gonzalez RC, Woods RE. Digital image processing. Prentice Hall; 2002.

[35] Riedl M. Optical design fundamentals for infrared systems. 2nd ed. Bellingham, WA: SPIE Press; 2001.

[36] Adelsberger K, Boye R, Zavislan J. Noise as a design constraint in broadband wavefront coded optical systems. International optical design conference. Optical design conference. Optical Society of America.; June 2014. IW1A-5.